

Alma Mater Studiorum Università di Bologna
Archivio istituzionale della ricerca

Polymer Photodetectors for Printable, Flexible, and Fully Tissue Equivalent X-Ray Detection with Zero-Bias Operation and Ultrafast Temporal Responses

This is the final peer-reviewed author's accepted manuscript (postprint) of the following publication:

Published Version:

Posar J.A., Davis J., Alnaghy S., Wilkinson D., Cottam S., Lee D.M., et al. (2021). Polymer Photodetectors for Printable, Flexible, and Fully Tissue Equivalent X-Ray Detection with Zero-Bias Operation and Ultrafast Temporal Responses. *ADVANCED MATERIALS TECHNOLOGIES*, 6(9), 1-10 [10.1002/admt.202001298].

Availability:

This version is available at: <https://hdl.handle.net/11585/871274> since: 2022-02-27

Published:

DOI: <http://doi.org/10.1002/admt.202001298>

Terms of use:

Some rights reserved. The terms and conditions for the reuse of this version of the manuscript are specified in the publishing policy. For all terms of use and more information see the publisher's website.

This item was downloaded from IRIS Università di Bologna (<https://cris.unibo.it/>).
When citing, please refer to the published version.

(Article begins on next page)

This is the final peer-reviewed accepted manuscript of:

Posar, J. A., Davis, J., Alnaghy, S., Wilkinson, D., Cottam, S., Lee, D. M., . . . Griffith, M. J. (2021). Polymer photodetectors for printable, flexible, and fully tissue equivalent X-ray detection with zero-bias operation and ultrafast temporal responses. *Advanced Materials Technologies*, 6(9)

The final published version is available online at:
<https://doi.org/10.1002/admt.202001298>

Terms of use:

Some rights reserved. The terms and conditions for the reuse of this version of the manuscript are specified in the publishing policy. For all terms of use and more information see the publisher's website.

This item was downloaded from IRIS Università di Bologna (<https://cris.unibo.it/>)

When citing, please refer to the published version.

**Polymer Photodetectors for Printable, Flexible and Fully Tissue Equivalent X-Ray
Detection with Zero-Bias Operation and Ultrafast Temporal Responses**

Jessie A. Posar,¹ Jeremy Davis,¹ Saree Alnaghy,¹ Dean Wilkinson,² Sophie Cottam,³ Donovan
M. Lee,³ Kristofer L. Thompson,³ Natalie P. Holmes,³ Matthew Barr,³ Adam Fahy,³ Nicolas
C. Nicolaidis,³ Fiona Louie,⁴ Beatrice Fraboni,⁵ Paul J. Sellin,⁶ Michael L. F. Lerch,¹ Anatoly
B. Rosenfeld,¹ Marco Petasecca,¹ Matthew J. Griffith^{3,7,*}

¹ Centre for Medical Radiation Physics, University of Wollongong, Wollongong, NSW, 2500,
Australia.

² Illawarra Cancer Care Centre, Wollongong Hospital, NSW 2500 Australia.

³ Priority Research Centre for Organic Electronics, University of Newcastle, Callaghan, NSW,
2308, Australia.

⁴ John Hunter Hospital, New Lambton Heights, NSW, 2305, Australia.

⁵ Department of Physics and Astronomy, University of Bologna, Viale Berti Pichat 6/2, 40127
Bologna, Italy

⁶ Department of Physics, University of Surrey, Guildford, Surrey GU2 7XH, UK.

⁷ School of Aeronautical, Mechanical and Mechatronic Engineering, University of Sydney,
Camperdown, NSW, 2006, Australia.

Corresponding Author Email: matthew.griffith@sydney.edu.au

Research interest in new materials for X-ray detection is growing rapidly, driven by demand from applications as diverse as fundamental materials science, medical imaging and radiotherapy, space exploration, security and defence, personal wearable dosimeters, and nuclear science.^[1-6] Current detectors utilize inorganic solid-state semiconductors such as silicon, selenium or cadmium zinc telluride. However, X-ray detectors fabricated from these materials are expensive to manufacture and cannot be easily fabricated into flexible sensors or large-area pixelated arrays.^[7] Furthermore, these semiconductors are composed of heavier elements, which exhibit much stronger X-ray attenuation than the lighter elements comprising human tissue, resulting in perturbation of the X-ray beam. Consequently, their use for medically relevant dosimetry or personal health monitoring requires complex, often unreliable calibrations limiting their applications in radiotherapy or food sterilization.^[8] A new generation of materials for X-ray sensing must therefore be envisaged, combining a tissue equivalent response with other ideal properties such as mechanical flexibility, low operating power requirements and real-time response rates.

Photoactive materials can be fabricated into either direct or indirect X-ray detectors. Direct detectors absorb X-rays and convert them into an electrical signal in a single photoconductor, whilst indirect detectors employ a scintillator to first convert X-rays to optical photons that are subsequently coupled into a secondary photodetector. Direct detectors face higher design constraints as the photoconductive materials must have both a high thickness for strong X-ray absorption and a high crystallinity for good charge carrier mobility. Thus, whilst recent developments with selenium, perovskite, and organic materials have produced high sensitivities ($S \sim 10^3\text{--}10^4 \mu\text{CGy}^{-1}\text{cm}^{-2}$),^[9-12] the thickness and crystallinity constraints mandate complex manufacturing and prevent radiation transmission, precluding their use in many applications. Indirect detectors offer more design flexibility, with the scintillator and

photodetector able to be independently optimized for X-ray absorption and charge carrier extraction, respectively. Consequently, indirect X-ray detectors have been the more widely adopted industrial architecture. However, state-of-the-art materials – including thallium-doped cesium iodide (CsI:Tl), terbium-doped gadolinium oxysulfide (GOS:Tb) or perovskite nanocrystals coupled to silicon photodetectors – are not tissue equivalent and require substantial bias voltages. Some of these materials also exhibit relatively slow response times due to delayed scintillator photoluminescence.

Organic semiconductors are a highly attractive pathway for creating devices that can circumvent each of the above limitations. Their use has become ubiquitous in multidisciplinary materials science due to the ability to tune their optoelectronic properties through simple wet chemistry procedures. They are also solution-processable, forming printable electroactive inks that enable cheap manufacturing onto flexible substrates at large scale.^[13-15] Such advantages have seen organic electronic materials and devices excel across a vast number of applications, including thin-film transistors,^[16] solar cells,^[17-20] sensors,^[21-22] visual displays,^[23-24] and photodetectors.^[25] Critically, the density of thin solid films fabricated from organic electroactive inks is very similar to that of human tissue, which has an approximate average value of 1.10 g cm^{-3} , and a value of 1.07 g cm^{-3} for the soft tissues most often encountered in medical dosimetry. These materials are therefore uniquely capable of tissue equivalent X-ray attenuation and electrical conductivity. Whilst organic semiconductors have been trialled as both photodetectors for indirect X-ray detection and photoconductors for direct detection, they have been found to be limited by low charge mobility (thus requiring application of bias voltages), very slow response times (thus limiting real-time X-ray detection) and poor photostability. These limitations can be addressed using the recent evolution of non-fullerene acceptors (NFAs). NFAs are broad spectrum light absorbers, a property which can also enable

versatile coupling with luminescence from different organic scintillators. Critically, their morphology and crystallinity can be controlled through synthetic chemical and device fabrication routes. Creation of planar NFA molecular structures can induce a high packing order, leading to both higher carrier mobility^[26-27] and enhanced stability against high energy irradiation.^[28] Combination of NFAs with a donor polymer creates a photodetector with a built-in electric field, thereby circumventing the requirement for an external bias to extract charge.

In this work we report the first ever demonstration of a printed X-ray detector that is fully tissue equivalent, has a rapid (sub-microsecond) response and exhibits good sensitivity at zero-bias operation. This performance is achieved by coupling an RP400 plastic scintillator with a photodiode composed of donor polymer P3HT and NFA o-IDTBR to create an indirect X-ray detector. We optimize fabrication conditions to provide both high carrier mobility and tuneable thickness for controlling radiolucency, enabling operation as a transparent dosimeter for wearable applications. Operation of the device with no external bias exhibits good sensitivity and a remarkably fast temporal response for X-ray detection, comparable to that of biased silicon photodetectors. The X-ray detecting materials system can be printed into flexible devices with pixel sizes of 60 μm that exhibit exceptional stability against aging degradation, repeated bending, and high irradiation doses – demonstrating a pathway for scalable production of large-area detector arrays.

Figure 1a shows geometry optimized chemical structures determined from quantum chemical modelling of the organic semiconductors. Both P3HT and o-IDTBR, like most organic semiconductors, consist predominantly of hydrogen and carbon with functional groups of other light elements; a similar elemental composition to human tissue. Since X-ray attenuation is determined by the electron densities of a material, achieving tissue equivalent X-ray detection requires the density of materials to be equivalent to human tissue, which has an approximate

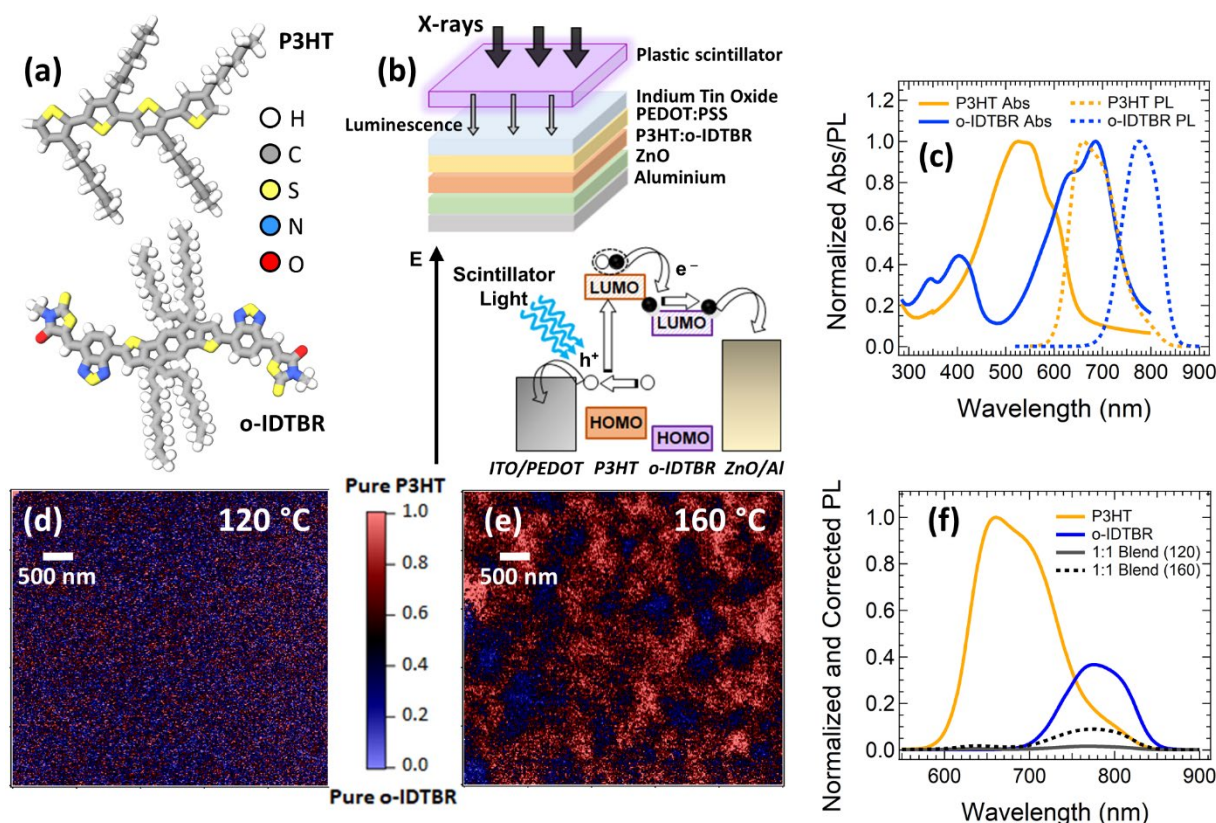


Figure 1: (a) Geometry optimized quantum chemical models of P3HT and o-IDTBR chemical structure. (b) The device architecture employed for the organic photodetector devices (that are the focus of this investigation) and the indirect X-ray detection experiments using a scintillator. The lower part of the figure shows the photodetector current transduction mechanism in response to luminescence from a scintillator. (c) UV-visible absorbance (solid) and photoluminescence (dashed) spectra for P3HT (orange) and o-IDTBR (blue). (d) STXM map of a blended P3HT:o-IDTBR film annealed at 120 °C for 10 minutes, and (e) 160 °C for 10 minutes after fabrication. Red pixels indicate pure P3HT phases and blue pixels indicate pure o-IDTBR phases. (f) A comparison of the photoluminescence spectra for pure P3HT (orange) and o-IDTBR (blue) films with blended films annealed at 120 °C for 10 minutes (grey) and 160 °C for 10 minutes (black and dashed) after fabrication.

value of 1.10 g cm^{-3} , and a value of 1.07 g cm^{-3} for the soft tissues most often encountered in medical dosimetry. Solid films cast from these organic semiconductors had mass densities of 1.04 g cm^{-3} for P3HT and 1.06 g cm^{-3} for o-IDTBR, highlighting their suitability for tissue-equivalent X-ray detection. Complete organic photodetectors fabricated using a 1:1 blend of P3HT:o-IDTBR for charge generation, PEDOT:PSS and ZnO for charge selective transport layers to prevent interfacial recombination, and ITO and aluminium electrodes (Figure 1b)

exhibited a mass density of 1.18 g cm^{-3} , confirming an excellent tissue equivalency for the fully fabricated organic photodetectors. Since many of these materials are solutions, they can be printed into a multilayer stack onto ITO-coated (120 nm) glass or ITO-coated flexible plastic anodes. This structure consists of a 40 nm hole-transporting PEDOT:PSS film, followed by deposition of the photoactive P3HT:o-IDTBR blend films (variable thickness) onto which a 30 nm ZnO electron transporting film is deposited. The device structure is then completed by vacuum deposition of a thin (100 nm) aluminium layer. Therefore, the entire device represents one of the first reported examples of a flexible X-ray detecting device with a fully tissue-equivalent response which can be fabricated with inexpensive printing technologies. These features are critical requirements for wearable detectors for safety and medical applications, since the device not only conforms to and provides a radiation response equivalent to the human body, but the low cross-section for X-ray absorption allows radiation transmission for applications requiring exposure to radiation without perturbing the energy fluence of the radiation.

P3HT exhibits a single broad absorption between 450 nm and 600 nm, whilst o-IDTBR shows both a blue (300-400 nm) and red absorption peak (550-750 nm) in comparison (Figure 1c). Collectively, the P3HT:o-IDTBR films exhibit optical absorption spanning the range of 300-750 nm, providing substantial versatility for coupling with X-ray absorbing scintillators. The photoluminescence spectra exhibit Stokes shifts of $\sim 120 \text{ nm}$ for each semiconductor, a signal which can be monitored to measure the extent of free charge generation efficiency in the blended film. The HOMO and LUMO energy levels of the materials are offset, allowing excitons generated in the low dielectric constant organic materials to be spontaneously dissociated into free charges at the material interfaces through a built-in electric field without the need for external bias, a process which causes quenching of the photoexcited states.^[29]

Smaller pure material domains promote this charge generation process, however larger and more crystalline domain sizes are typically advantageous for fast carrier transport through the film. To optimise the internal blend nanostructure, films were subjected to various thermal treatments to induce crystallinity and domain size changes. The size of material phases was determined using scanning X-ray transmission microscopy (STXM) measurements performed at the Advanced Light Source (ALS) synchrotron, while the charge generation efficiency was monitored by comparing the residual photoluminescence in the blended films to that of the individual materials. STXM provides high-resolution (~25 nm) imaging with chemical sensitivity to collect X-ray maps of the blend morphology. A range of different thermal post-treatment conditions were trialled with annealing at 120 °C for 10 minutes found to produce the best films, which exhibited strongly intermixed morphology below the resolution limit of the technique (Figure 1d). Photoluminescence in these blended films was negligible, with a calculated quantitative charge generation yield of 98% (Figure 1f), whilst the fine structure of the absorbance spectrum suggests some crystallinity. Increasing the annealing temperature to enhance polymer crystallinity caused gross phase segregation, where the individual domain sizes became much larger than the ~20 nm exciton diffusion length (Figure 1e). This segregation resulted in poorer exciton dissociation, with the generation yield decreased to 72% as determined from photoluminescence quenching (Figure 1f). Fabrication conditions producing the optimized nanoscale morphology were utilised for the remainder of the study to maximize sensitivity for X-ray detection.

Figure 2a shows the current density–voltage (J – V) characteristics of photodetector devices with P3HT:o-IDTBR thicknesses ranging from 100 nm to 7 μm. For thicknesses above 100 nm, the data reveals nearly complete charge extraction at ultra-low (and even zero) applied bias, with minimal differences in the photocurrent extracted in passive mode (0 V) and at -5 V bias. This

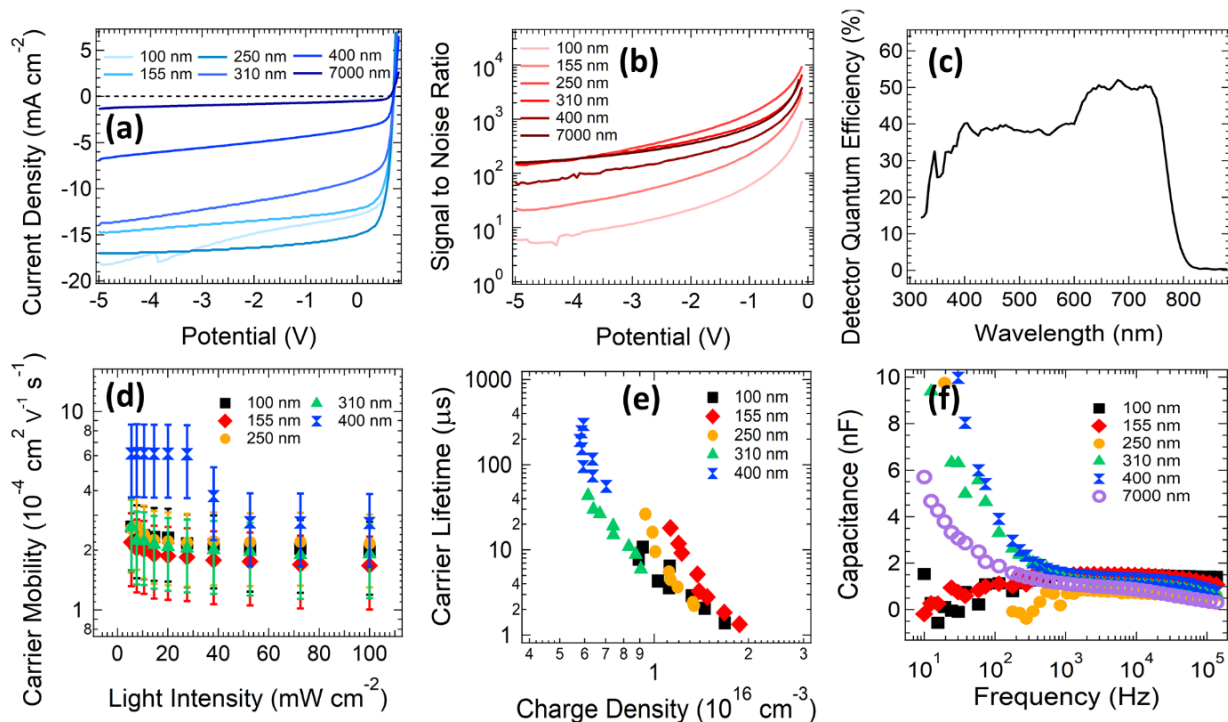


Figure 2: (a) Current density-voltage curves for P3HT:o-IDTBR photodetectors with thicknesses between 100 nm and 7000 nm. (b) Photocurrent to dark current signal to noise ratios for devices as a function of the applied bias. (c) The detector quantum efficiency for optical to electrical conversion as a function of wavelength in the 250 nm device, (d) Charge carrier mobility in photodetectors as a function of their light intensity at various thicknesses. (e) Charge carrier lifetime as a function of the photogenerated charge density in photodetectors. (f) Photodetector capacitance as a function of perturbation AC voltage frequency for photodetectors operating under illumination without any DC bias voltage.

result demonstrates that these printable P3HT:o-IDTBR devices are extremely efficient at extracting generated charges without requiring external bias, a key advantage in wearable electronic devices. Comparing the photocurrent to the dark current demonstrates exceptional signal-to-noise ratios (SNRs) of 10^3 to 10^4 at bias voltages below -0.5 V for film thicknesses of 250 nm to 7 μm (Figure 2b). These values are equivalent to state-of-the-art silicon photomultiplier detectors, but without requiring the same high bias voltages (> 25 V) as inorganic semiconductors. Light absorption was found to be maximized after a thickness of 250 nm had been reached (Figure S1), corresponding with the thickness value that produced the best optical-to-electrical power conversion efficiency (Table S2). The quantum efficiency for converting optical photons into current was constant at a value of $\sim 40\%$ between 400 nm

and 600 nm (Figure 2c), a spectral range which covers the luminescence light outputs of the vast majority of commercially available X-ray scintillators (vide infra).

Charge carrier dynamics were measured to provide comprehensive insight into material nanostructure and aid in optimizing their performance in a coupled indirect X-ray detection system. The device charge carrier mobility was determined to be between $2\text{--}3 \times 10^{-4} \text{ cm}^2\text{V}^{-1}\text{s}^{-1}$ from current transients using photo-CELIV measurements (Figure S1), with this mobility invariant for all thicknesses up to 400 nm (Figure 2d). The photo-CELIV technique produces an ambipolar mobility influenced by both hole and electron transport, however, this mobility value is dominated by the faster carrier for imbalanced transport, which has been reported to be the holes for this P3HT:o-IDTBR system in previous studies.^[30] The increase in photoactive layer thickness from 400 nm to 7000 nm substantially increased the series resistance of the devices, resulting in a significant increase in the RC time constant of the devices (from <500 ns to 2.2 μs , see Table S1). The longer RC time constant prevented accurate current extraction and mobility determination in these thicker 7000 nm films, as the device response became slower than the lifetime of charges (Figure 2e). Consequently, photophysical parameters extracted from the transient measurements have not been plotted for this thickness in Figures 2d, e and f. The carrier mobility determined for the P3HT:o-IDTBR system is an order of magnitude higher than that previously observed in organic polymer systems that have been trialled as photodetectors for X-ray detection (P3HT:PCBM = $4.4 \times 10^{-5} \text{ cm}^2\text{V}^{-1}\text{s}^{-1}$), thus allowing improved performance and detection sensitivity.^[31] Indeed the P3HT:o-IDTBR devices fabricated here have the highest photocurrents reported for any organic photodetector systems employed for indirect detection of X-rays. The enhanced carrier mobility is attributed to the combination of the highly planar o-IDTBR acceptor with a P3HT donor that exhibits high regioregularity along the thiophene sidechains (Figure 1a), promoting the formation of

217 highly ordered crystalline domains that provide higher charge carrier mobility. The charge
218 carrier lifetime was found to vary between 1 and 100 μs depending on the photoinduced charge
219 density (light intensity) and film thickness (with increasing charge density causing a greater
220 concentration of charge carriers and thus faster recombination (Figure 2e). However, the
221 gradient of the lifetime vs charge density plots were not affected by the thickness of the
222 photoactive materials within the range of 100 nm to 400 nm, suggesting that the recombination
223 rate is unaffected by device thickness, and thus implying that the nanoscale morphology of the
224 blends does not meaningfully change over this thickness range. The distribution of charge
225 trapping states within the blend morphology was investigated by electrochemical impedance
226 spectroscopy, with devices operating under illumination at short circuit perturbed by a small
227 AC voltage to determine how carriers within the device respond. As presented in Figure 2f, all
228 mobile charges – which are detected by their characteristic response to faster probe perturbation
229 frequencies (10^3 - 10^4 Hz) – were extracted efficiently for all thicknesses, resulting in only the
230 geometric device capacitance. However, more deeply trapped charges, which respond when
231 the perturbation frequency is lowered to less than 10^2 Hz, became trapped inside devices for
232 film thicknesses between 310 nm and 7 μm , as determined by the rapidly increasing
233 capacitance at these lower frequencies. This result implies that operation without external bias
234 will not efficiently extract photoinduced charges for device thicknesses exceeding 310 nm,
235 providing an upper bound on the photodetector thickness for zero-bias operation. This value
236 precludes the use of these particular organic semiconductors as direct X-ray detectors, as this
237 low thickness would result in a lower sensitivity (vide infra). Consequently, these thin organic
238 films are highly compatible with creation of a flexible, radiolucent material system for the
239 photodetector component of an indirect X-ray detector. These photodetectors can be operated
240 without external bias but still achieve fast temporal responses, as the carriers are only required
241 to transit distances of less than 0.3 μm .^[30, 32] We note that there have been other reports of

organic semiconductors used as direct X-ray detectors with high sensitivities, however, these devices do not produce any X-ray detection without external power.^[11-12, 33]

Complete X-ray detectors were fabricated by coupling the P3HT:o-IDTBR photodetectors with a 2 mm thick plastic scintillator to absorb X-rays and produce visible light with a peak at 425 nm (Figure S4). The mass density of the plastic scintillator is 1.023 g cm⁻³, with an electron density of 3.33x10²² cm⁻³, compared to values of 1.07 g cm⁻³ and 3.34x10²² cm⁻³, respectively, for soft tissue. Thus the addition of the plastic scintillator enables the device to maintain its

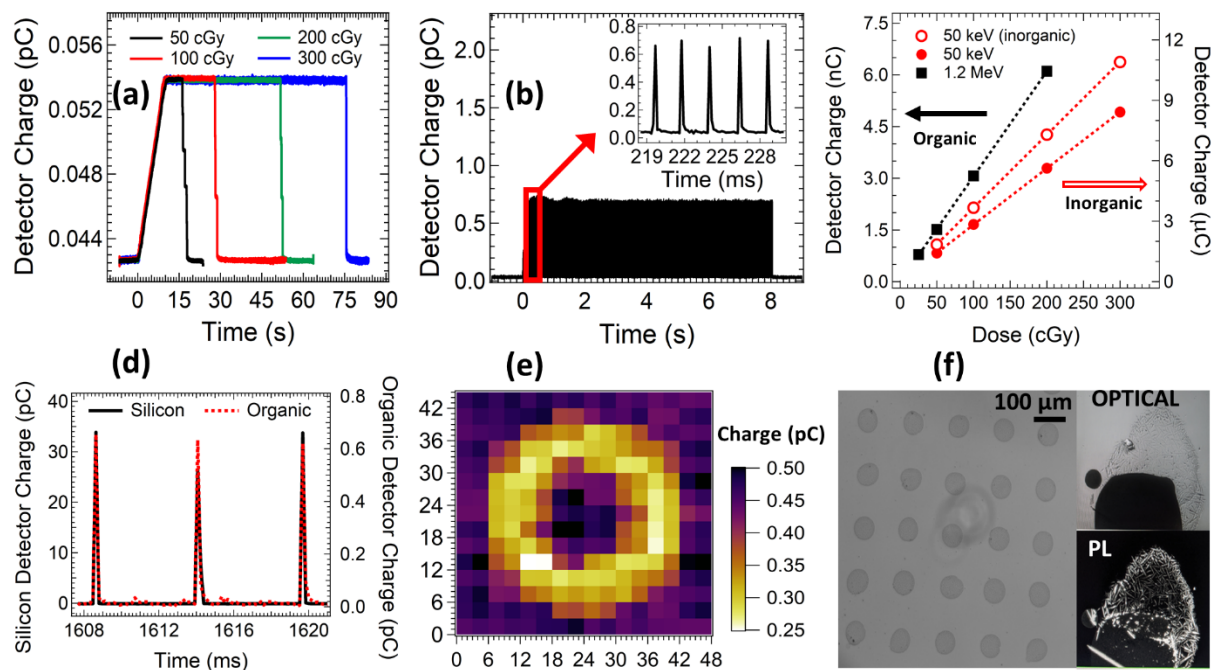


Figure 3: (a) Indirect detection of $\langle E \rangle = 50$ keV X-rays at various cumulative doses, and (b) $\langle E \rangle = 1.2$ MeV X-rays using a 2 mm plastic scintillator coupled to the P3HT:o-IDTBR photodetectors. The inset in (b) presents an expanded view to show the resolution of individual 3.6 μ s pulses. (c) The coupled X-ray detection system response as a function of radiation dose at 50 keV (red) and 1.2 MeV (black). The response of the photodetector coupled with a 2 mm LYSO inorganic scintillator is shown in open red circles for reference purposes. (d) A comparison of the temporal response for detection of 3.6 μ s pulses at $\langle E \rangle = 1.2$ MeV for silicon (black) and the coupled organic X-ray detector (red dashed). (e) An X-ray image of a standard metal washer acquired with the organic X-ray detector under the 50 keV X-ray beam. (f) An image of an inkjet-printed array of scintillator dots deposited onto organic photodetectors with pixel pitch of 120 μ m. Zoomed in optical and photoluminescence (PL) microscope images of a single pixel show quenching of the photoluminescence in the area of overlap between the scintillator and the photodetector, indicating normal operation of the coupled detection system in the printed array.

tissue equivalent X-ray attenuation properties.^[34] The electrical response to X-ray irradiation was measured in zero-bias operation for both low (keV) and high (MeV) X-ray energies to explore the organic material applicability across a range of applications. The low energy response was investigated with X-rays produced from a clinical X-ray tube radiating a dispersive X-ray beam with mean energy of $\langle E \rangle = 50$ keV. The tube required a long ramp time (~ 10 s) to reach the maximum machine rate output, which was detected by the coupled scintillator/photodiode system as shown in Figure 3a by the rising edge of the detector charge profile. The electrical response increased linearly with the X-ray dose deposited from 50 cGy to 300 cGy (Figure 3c).

Each profile in Figure 3a was repeated three times, showing exceptional reproducibility (error bars in Figure 3c, defined as one standard deviation, are smaller than the marker size). The sensitivity for X-ray detection, calculated from the gradient of the data in Figure 3c, was determined to be $1.6 \times 10^4 \mu\text{CGy}^{-1}\text{cm}^{-3}$. This value is somewhat lower than other organic X-ray detection systems, though remains noteworthy as it is obtained without any bias and matches that of state-of-the-art amorphous selenium direct detectors used in current medical imaging technologies ($\sim 1 \times 10^4 \mu\text{CGy}^{-1}\text{cm}^{-3}$). Furthermore, the sensitivity was found to be restricted by the plastic scintillator required for full tissue equivalency rather than the intrinsic photodetector performance. The RP400 plastic scintillator generates a relatively low light yield (9,200 photons MeV^{-1}) and has a limited emission spectral overlap with the photodetector absorption (Figure 1c and S4) in comparison to inorganic scintillators. Coupling the photodetector to an inorganic LYSO (Lutetium-yttrium oxyorthosilicate) scintillator, which is employed in existing reference technologies and has both a higher light yield of 33,200 photons MeV^{-1} and a broader spectral overlap between the scintillator emission and the P3HT:o-IDTBR absorption in the range of 500-600 nm, produces a sensitivity of $3.6 \times 10^7 \mu\text{CGy}^{-1}\text{cm}^{-3}$, a value

more than three orders of magnitude higher than that produced with the plastic scintillator and equivalent to the best indirect X-ray detecting sensitivities reported with organic photodetectors.^[35-36] The response to high energy X-rays produced from a Varian Clinac® 21iX linear accelerator operating at 6 MV ($\langle E \rangle = 1.2$ MeV) used for radiotherapy treatment of cancer showed similar sensitivity to that observed in the lower energy keV X-rays, but with a completely different temporal response. The electrical output was again found to be linear with increasing X-ray dose, with a calculated sensitivity of $3.4 \times 10^4 \mu\text{CGy}^{-1}\text{cm}^{-3}$ with the plastic scintillator and a response that saturated our detector with the inorganic LYSO scintillator. We also monitored the transmission of the photodetector and scintillator to high and low energy X-rays beams (Figure S5 and Table S2). The native transmission of the photodetector was extremely high 99.8% ($\pm 0.1\%$) under the 6 MV linac beam, dropping slightly to 84.9% ($\pm 0.2\%$) for the low energy X-rays, likely due to stronger interactions with the ITO-glass substrate at lower energies. Addition of the scintillator decreased transmission by 0.2% for high energy and 1.5% for low energy X-rays. These results confirm the high radiolucency of these devices and their applicability for wearable dosimetry applications.

Of particular interest, the detection response for the MeV X-rays shows a remarkably fast temporal resolution. The linear accelerator is a pulsed radiation source with a pulse width of 3.6 μs and an instantaneous dose delivery of 270 μGy per pulse. Figure 3b shows that the tissue equivalent X-ray detectors can resolve each individual pulse generated from the linear accelerator, and rapidly discharges completely following each pulse. This result confirms that the temporal response of this organic photodetector is at least an order of magnitude faster than that typically reported for other organic semiconductor systems. A comparison of the timing response of the organic device with a state-of-the-art silicon radiation detector in Figure 3d shows negligible differences in the risetime and discharge performance between these two

technologies, indicating that both sensors can follow the time structure of these fast X-ray pulses with similar performance, though direct comparison of the respective limiting time responses would require a faster pulsed energy source. These results show for the first time that judicious material choice and optimisation of organic semiconductor device architecture produces organic photodetector devices that can follow the temporal profile of fast pulsed X-ray sources, in contrast to previously reported limitations with low carrier mobilities.^[26] The increased mobility enabling an organic photodiode that can follow the pulsed X-ray beam profile with similar performance to silicon is supported by consideration of the carrier transit time as an approximation for temporal response. The transit time of carriers through the film is given by $t_{tr} = \frac{L}{v}$, where L is the photoactive film thickness and v the carrier velocity. Since the carrier velocity is related to mobility according to $v = \mu E_{bi}$, where μ is the mobility and E_{bi} is the magnitude of the built-in field created by the asymmetric electrode work functions, calculated here as $E_{bi} = \frac{V_{oc}}{L}$ where V_{oc} is the open circuit voltage, the transit time is related to mobility according to $t_{tr} = \frac{L^2}{\mu V_{oc}}$. For a 250 nm film, using the μ (increased by an order of magnitude compared to previous organic blends) and V_{oc} values for these photodetectors extracted from Figure 2, a transit time of 1.9 μ s is calculated, in agreement with the measured charge extraction times in Figure S3 and confirming the organic photodiodes can respond to the fast X-ray beam pulses without delay. To test the applicability of the device in standard X-ray detection applications, multiple 2 x 2 mm pixels were used to acquire a 2D X-ray scan of a flat aluminium annulus-shaped washer. The X-ray image shows high contrast (Figure 3e), with the spatial resolution limited only by the photodetector pixel dimensions. The successful acquisition of an X-ray image demonstrates the functionality of the new P3HT:o-IDTBR photodetector. Further attention can now be directed at improving the device design and manufacture to optimise performance.

340

341 Figure 3f shows an image of organic photoactive materials printed into a pixelated array
342 covered with a second layer of a printable organic scintillator (1-phenyl-3-mesityl-2-
343 pyrazoline) to create 60 μm electroactive dots with a centre-to-centre pixel pitch of 120 μm .
344 This result demonstrates the ability to produce detectors that have 2D detection properties, with
345 a spatial resolution of the same order as state-of-the-art inorganic detection arrays (typically 98
346 μm pitch), but with the enticing ability to scale the detector array quickly and cheaply to much
347 larger sizes than current X-ray arrays are capable of achieving. The functionality of the printed
348 array was investigated with optical and photoluminescence microscopy, focusing on a pixel
349 where the scintillator (light colour in optical image) is deliberately offset from the organic
350 photodetector (dark colour). The photoluminescence microscopy confirms the scintillator is
351 highly fluorescent, however, this fluorescence disappears in regions of the printed pixel where
352 the scintillator overlaps with the photodetector. This result could simply be attributed to
353 absorbance of the emitted light from the photodetector materials, or alternatively, could also
354 arise from loss of fluorescence in the scintillator due to efficient transfer of the optical energy
355 to the organic photodetector component as we have observed in similar materials systems.^[37]
356 Whilst the former explanation does not provide insight into device functionality, the latter
357 explanation would be indicative of a fully functional organic indirect X-ray detection system
358 that can be fabricated with inexpensive printing techniques into spatially resolved flexible
359 arrays. This ability to form thin flexible arrays is highly advantageous for wearable dosimetry
360 applications where the target area shifts due to the movement of the human body.

361

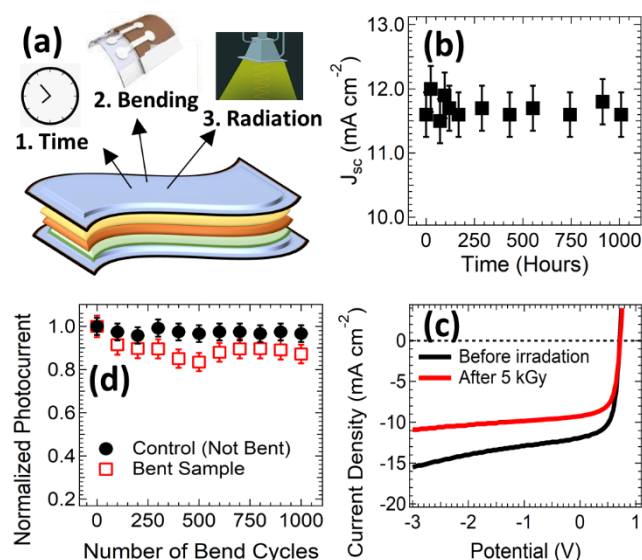


Figure 4: (a) An illustration of the three different degradation mechanisms to which the flexible organic photodetectors were subjected. (b) Detector photocurrent as a function of time. (c) Detector photocurrent as a function of the number of repeated bend cycles (red) around a radius of 1 cm. The control data for an unbent sample is shown in black. (d) The current density-voltage curves for photodetectors before (black) and after (red) 5kGy irradiation from a ⁶⁰Co source.

The stability of the flexible X-ray photodetectors was assessed against 3 different degradation mechanisms; time, repeated mechanical flexing, and large radiation doses (Figure 4a). The organic materials were protected from air and water using a flexible barrier film composed of polyethylene terephthalate (PET) stacks integrated with a commercial UV and moisture barrier (Amcor UB4) and barrier resin glue to minimize oxidation of the semiconductors in the sensitive volume. PET films are known to exhibit scintillation with a deep blue photon emission, potentially overlapping with that of the RP400 plastic scintillator employed in the devices.^[38] We have extensively characterised the influence of these barrier films on the sensitivity and radiation hardness of organic photodiodes elsewhere, confirming that they have minimal effects on both parameters.^[39] No degradation in performance was observed after encapsulation for up to 1000 hours, within the measurement error margin of 4% (Figure 4b). Photodetector performance was tested with a voltage cycle between +1V and -5V every day for the first 5 days, then every 100 hrs thereafter. Light intensity during measurements was 100

383 mWcm⁻², with a total light exposure time of approximately 1 hour over the testing period,
384 followed by storage in a dark, air permeable environment. This intense level of light exposure
385 is orders of magnitude higher than that produced from the plastic scintillator under X-ray
386 exposure, providing an accelerated testing platform that implies a long device shelf-life under
387 continuous operation. The stability of the photodetector current output during repeated bending
388 cycles was tested by preparing new encapsulated devices with similar organic materials
389 prepared using home-made synthesis procedures to fit the flexible testing apparatus. Devices
390 were taken from flat to a bend radius of 1 cm and monitoring performance after every 100
391 cycles, was tested by assembling new form similar materials. is shown in Figure 4c. The
392 photocurrent output decreased by a total of 12% after 1000 bending cycles, confirming the high
393 stability of the organic photodetectors against mechanical stress. No visual evidence of
394 interfacial fracture was observed in any of the samples measured. Finally, the stability of the
395 photodetector to harsh irradiation conditions was investigated, a property for which previous
396 studies have found organic semiconductors have particularly poor performance. Dosimeters
397 for medical applications may be exposed to X-ray doses as high as 500 Gy per year and are
398 expected to perform with minimal degradation. Plastic scintillators, such as the one used in this
399 study, have been extensively characterized for high energy physics applications and proven to
400 exhibit high radiation hardness, with less than 8% variation in their light yields up to an
401 irradiation of 10 kGy.^[40-41] Therefore, the P3HT:o-IDTBR photodetector response was
402 characterized independently after irradiation with a cobalt-60 gamma source up to a total
403 irradiation dose of 5 kGy (approximately equivalent to a 5 year working lifetime in high dose
404 applications, and 10 years in medical imaging). A decrease in the photocurrent output of 22%
405 was observed for zero-bias operation after 5 kGy of irradiation (Figure 4d). This result is
406 exceptional for organic semiconductors, representing not only the first report on the effect of
407 ionizing radiation for organic non-fullerene acceptor materials, but also one of the best

radiation hardness results reported, with less than half the degradation of other solution-based organic semiconductors at the same level of irradiation.^[42] This result substantiates one of the rationales for employing the planar NFA material o-IDTBR, which was a suspected increased resistance to radiation-induced degradation. The suspected origin of the enhanced radiation tolerance is the strong degree of planarity in the molecular structure of o-IDTBR. Recent work has found that these non-fullerene acceptor molecules undergo a photoinduced conformational change as a key initiator of photooxidation and subsequent degradation, further reporting that if this planarity was frozen by the use of molecular interactions or structure it would be possible to inhibit the degradation.^[43] Furthermore, the optical-to-electrical conversion efficiency of photodetectors fabricated with the NFA were already greater than any other reported polymer-based materials employed in X-ray detecting systems, showing at least double the initial performance of other systems such as P3HT:PCBM, F8BT:PDI or TFB:PDI.^[44] Thus the performance of the P3HT:o-IDTBR photodetectors not only make them the most efficient polymer-based organic materials used in indirect X-ray detectors by up to an order of magnitude after irradiation, but they also maintain a higher performance after irradiation than any other pristine non-irradiated polymer-based devices have ever achieved.

To conclude, we have demonstrated a new printable organic material combination for the photodetector component of an indirect X-ray detection system. The device exhibits exceptional optical-to-electrical conversion efficiency as a photodetector, with higher performance than any other reported printable organic systems and the unique ability to operate efficiently with zero external bias. Complete X-ray detectors fabricated by coupling the photodiode with a plastic scintillator are amongst the first flexible and fully tissue equivalent X-ray detectors capable of operating without external bias. The X-ray performance is energy independent between 50 keV and 1.2 MeV, with a detection sensitivity that is equivalent to

inorganic direct X-ray detectors for the pulsed beams monitored and the fastest temporal response ever reported for organic indirect X-ray detectors. The materials can be printed into a pixelated array to provide high spatial resolution and demonstrate major improvements in both radiation hardness and temporal response compared to other organic materials. The device is also shown to be highly stable with respect to time, mechanical flexing and large radiation doses. The new materials and fully tissue equivalent X-ray detectors we report here provide a device that is capable of being a stable, printable, flexible, and tissue equivalent detector with high radiolucency for wearable applications where simultaneous monitoring and transmission of the X-ray absorbed dose in the human body is required.

Experimental

Device Fabrication: ITO-coated glass and ITO-PET substrates were employed as anodes after cleaning by successive ultrasonication in acetone, isopropyl alcohol and deionized water, followed by 15 min of UV-ozone treatment. PEDOT:PSS suspensions (Heraeus) were filtered (0.45- μ m), deposited onto electrodes by spin-coating at 4000 rpm for 90 s, then annealed at 140 °C for 30 min, producing 40 nm films. P3HT:o-IDTBR films (1:1 ratio) were deposited from 10 mg mL⁻¹, 18 mg mL⁻¹ and 30 mg mL⁻¹ solutions in chloroform by spin-coating in a glove box at a variety of speeds to obtain the desired thickness, followed by drying at 70 °C for 4 min. Zinc oxide (10 mg mL⁻¹ in acetone) was deposited at 5000 rpm for 50 s, followed by drying at 80 °C for 2 min, producing 40 nm films. A 100 nm aluminum metal contact was thermally evaporated (Angstrom Amod) in a vacuum with a chamber pressure of 2 x10⁻⁶ Torr and area of 4 mm², followed by annealing of the completed devices at 120 °C for 10 min. The devices were encapsulated by a barrier film (Amcor; UB4 + UV) and epoxy glue (DELO LP655) with a 30 s exposure under a UV lamp to seal the device.

Optoelectronic Characterization: J - V measurements were performed in the dark and under an AM1.5 white light spectrum using a Keithley 2400 sourcemeter. External Quantum Efficiency (EQE) measurements were achieved using illumination from a mechanically chopped 100 W quartz tungsten halogen lamp passed through an Oriel Cornerstone 130 monochromator. Photocurrent responses were measured with a digitizing lock-in amplifier and referenced to a calibrated silicon diode. UV-vis absorbance spectra were measured using the Cary 6000i UV-vis Spectrophotometer with a Diffuse Reflectance Accessory (DRA-1800), with the defined thicknesses of the sensitive volume spun on quartz slides. Photoluminescence spectra were acquired using a Varian Cary Eclipse fluorescence spectrophotometer with an excitation wavelength of 400 nm.

X-Ray Response Characterization: X-ray characterization was achieved at the Illawarra Cancer Care Centre at Wollongong Hospital, Australia. The device was attached to a thin PCB probe and read out using a custom-designed data acquisition system based on a DDC264 chip in passive mode. A 2 mm thick plastic scintillator (Rexon; RP400) was coupled to the back of the device with coupling grease (RX-688) and wrapped in Teflon tape to reduce reflections. Two beam sources were used: (a) a Gumlay orthovoltage X-ray tube with a broad 100 kVp spectrum ($\langle E \rangle = 50$ keV), with the device at surface and 30 cm from the source, and (b) a Varian Clinac® 21iX linear accelerator (Varian Medical Systems, Palo Alto, USA) pulsed radiation source producing 6 MV photons ($\langle E \rangle = 1.2$ MeV) with a pitch of 3.6 μ s and repetition rate of 360 Hz, with an instantaneous dose rate of 2.5 kGy/min. The device for source (b) was placed at a source-to-surface distance of 100 cm at a sample depth of 1.5 cm in a water-equivalent plastic phantom.

Charge Carrier Dynamics: Photo-CELIV, TPV and impedance measurements were performed using the commercially available PAIOS 2 system (Fluxim AG). For carrier transport and recombination data, a light pulse from a white LED (Cree, xp-g) was used to generate charges whilst a compensating offset voltage held the device at open circuit. The end of the light pulse was simultaneous with the application of either a linearly increasing voltage (photo-CELIV) or square-step voltage (TPV) to extract photogenerated charges. The current transients were recorded by the integrated PAIOS hardware. The impedance response was measured over the range of 10 Hz to 1 MHz with an oscillation amplitude of 30 mV. The impedance was recorded under dark and illuminated conditions at 0 V applied bias (short circuit conditions).

STXM Microscopy: STXM measurements were performed on beamline 5.3.2.2 at the ALS synchrotron. Samples were prepared for STXM measurements by spin coating 2.5 μL of nanoparticle ink onto low stress silicon nitride (Si_3N_4) membrane windows with silicon dioxide coating (window dimensions $0.25 \times 0.25 \text{ mm}^2$, window thickness 15 nm, silicon frame dimensions $5 \times 5 \text{ mm}^2$, purchased from Norcada, Canada) at 3000 rpm, 1 min, low acceleration of 112 rpm/s. Samples were air dried at room temperature. The samples on Si_3N_4 windows were loaded in the STXM sample chamber and rastered with respect to the X-ray beam. The STXM sample chamber was backfilled with helium (0.33 atm). The transmitted X-ray beam is detected by a scintillator and a photomultiplier tube. The STXM Fresnel zone plate had an outer most zone width of 25 nm, setting the spatial resolution limit of the measurement. A careful selection of the photon energy for each X-ray (NEXAFS) spectrum was performed, establishing orthogonal energies to uniquely identify both P3HT and o-IDTBR. Singular value decomposition was used to fit a sum of the pristine material NEXAFS spectra to the measured blend spectrum of the nanoparticles – at each pixel – in the STXM images. The aXis2000 package was used to perform image analysis of STXM maps.

Acknowledgements: This work was performed in part at the Materials node of the Australian National Fabrication Facility, a company established under the National Collaborative Research Infrastructure Strategy to provide nano- and microfabrication facilities for Australia's researchers. This research used resources of the Advanced Light Source, which is a DOE Office of Science User Facility under contract no. DE-AC02-05CH11231. The authors thank support staff at the Advanced Light Source synchrotron and the Illawarra Cancer Care Centre. NH, MB and AF acknowledge travel funding provided by the International Synchrotron Access Program (ISAP) managed by the Australian Synchrotron, part of ANSTO, and funded by the Australian Government. MG acknowledges funding for this work through a Strategic Investment grant from the University of Newcastle (10.32385). JP acknowledges the Australian Government Research Training Program Scholarship and the Australian Institute of Nuclear Science and Engineering (AINSE) Post-Graduate Research Award for funding this work.

References:

- [1] M. J. Griffith, S. Cottam, J. Stamenkovic, J. A. Posar, M. Petasecca, *Frontiers in Phys.*, **2020**, 8.
- [2] B. Fraboni, A. Fraleoni-Morgera, N. Zaitseva, *Adv. Mater.*, **2016**, 26, 2276.
- [3] S. Peracchi, N. Matsufuji, A. Kok, M. Povoli, M. Jackson, A. B. Rosenfeld, L. T. Tran, B. James, D. Bolst, D. A. Prokopovich, J. A. Davis, S. Guatelli, M. Petasecca, M. L. F. Lerch, *IEEE Trans. Nuclear Sci.*, **2020**, 67, 169.
- [4] X. Xu, J. Chen, S. Cai, Z. Long, Y. Zhang, L. Su, S. He, C. Tang, P. Liu, H. Peng, X. Fang, *Adv. Mater.*, **2018**, 30, e1803165.
- [5] N. Kotwaliwale, K. Singh, A. Kalne, S. N. Jha, N. Seth, A. Kar, *J. Food Sci. Technol.*, **2014**, 51, 1.
- [6] M. J. Griffith, N. A. Cooling, D. C. Elkington, E. Muller, W. J. Belcher, P. C. Dastoor, *Appl. Phys. Lett.*, **2014**, 105, 143301.
- [7] L. Basirico, A. Ciavatti, T. Cramer, P. Cosseddu, A. Bonfiglio, B. Fraboni, *Nat. Commun.*, **2016**, 7, 13063.
- [8] J. A. Posar, J. Davis, M. J. Large, L. Basirico, A. Ciavatti, B. Fraboni, O. Dhez, D. Wilkinson, P. J. Sellin, M. J. Griffith, M. L. F. Lerch, A. Rosenfeld, M. Petasecca, *Med. Phys.*, **2020**, 47, 3658.
- [9] H. Wei, J. Huang, *Nat. Commun.*, **2019**, 10, 1066.

- 540 [10] A. Ciavatti, E. Capria, A. Fraleoni-Morgera, G. Tromba, D. Dreossi, P. J. Sellin, P.
541 Cosseddu, A. Bonfiglio, B. Fraboni, *Adv. Mater.*, **2015**, 27, 7213.
- 542 [11] H. M. Thirimanne, K. Jayawardena, A. J. Parnell, R. Bandara, A. Karalasingam, S.
543 Pani, J. E. Huerdler, D. G. Lidzey, S. F. Tedde, A. Nisbet, C. A. Mills, S. Silva, *Nat.*
544 *Commun.*, **2018**, 9, 2926.
- 545 [12] I. Temino, L. Basirico, I. Fratelli, A. Tamayo, A. Ciavatti, M. Mas-Torrent, B. Fraboni,
546 *Nat. Commun.*, **2020**, 11, 2136.
- 547 [13] M. J. Griffith, N. A. Cooling, B. Vaughan, D. C. Elkington, A. S. Hart, A. G. Lyons, S.
548 Qureshi, W. J. Belcher, P. C. Dastoor, *IEEE J. Selected Topics Quant. Electron.*, **2016**,
549 22, 1.
- 550 [14] T. R. Andersen, F. Almyahi, N. A. Cooling, D. Elkington, L. Wiggins, A. Fahy, K.
551 Feron, B. Vaughan, M. J. Griffith, A. J. Mozer, C. Sae-kung, G. G. Wallace, W. J.
552 Belcher, P. C. Dastoor, *J. Mater. Chem. A*, **2016**, 4, 15986.
- 553 [15] M. J. Griffith, N. A. Cooling, B. Vaughan, K. M. O'Donnell, M. F. Al-Mudhaffer, A.
554 Al-Ahmad, M. Noori, F. Almyahi, W. J. Belcher, P. C. Dastoor, *Energy Technol.*, **2015**,
555 3, 428.
- 556 [16] H. Klauk, *Chem. Soc. Rev.*, **2010**, 39, 2643.
- 557 [17] G. C. Welch, M. Leclerc, *Chem. Rec.*, **2019**, 19, 961.
- 558 [18] C. J. Brabec, J. R. Durrant, *MRS Bull.*, **2008**, 33, 670.
- 559 [19] M. Marks, N. P. Holmes, A. Sharma, X. Pan, R. Chowdhury, M. G. Barr, C. Fenn, M.
560 J. Griffith, K. Feron, A. L. D. Kilcoyne, D. A. Lewis, M. R. Andersson, W. J. Belcher,
561 P. C. Dastoor, *Phys. Chem. Chem. Phys.*, **2019**, 21, 5705.
- 562 [20] M. Ameri, M. Al-Mudhaffer, F. Almyahi, G. C. Fardell, M. Marks, A. Al-Ahmad, A.
563 Fahy, T. Andersen, D. C. Elkington, K. Feron, P. C. Dastoor, M. J. Griffith, *ACS Appl.*
564 *Mater. Interfaces*, **2019**, 11, 10074.
- 565 [21] M. J. Griffith, M. Willis, P. Kumar, J. L. Holdsworth, H. Bezuidenhout, X. Zhou, W. J.
566 Belcher, P. C. Dastoor, *ACS Appl. Mater. Interfaces*, **2016**, 8, 7926.
- 567 [22] W. Huang, L. Feng, G. Wang, E. Reichmanis, in *Flexible and Wearable Electronics for*
568 *Smart Clothing*, Wiley-VCH, USA, 1-27, **2020**.
- 569 [23] S. Reineke, F. Lindner, G. Schwartz, N. Seidler, K. Walzer, B. Lüssem, K. Leo, *Nature*,
570 **2009**, 459.
- 571 [24] H. W. Chen, J. H. Lee, B. Y. Lin, S. Chen, S. T. Wu, *Light Sci. Appl.*, **2018**, 7, 17168.
- 572 [25] P. C. Y. Chow, T. Someya, *Adv. Mater.*, **2020**, 32, e1902045.
- 573 [26] H. Fu, Z. Wang, Y. Sun, *Angew. Chem. Int. Ed.*, **2019**, 58, 4442.
- 574 [27] R. S. Gurney, D. G. Lidzey, T. Wang, *Rep. Prog. Phys.*, **2019**, 82, 036601.
- 575 [28] E. M. Speller, A. J. Clarke, J. Luke, H. K. H. Lee, J. R. Durrant, N. Li, T. Wang, H. C.
576 Wong, J.-S. Kim, W. C. Tsai, Z. Li, *J. Mater. Chem. A*, **2019**, 7, 23361.

577 [29] J. Hou, O. Inganas, R. H. Friend, F. Gao, *Nat. Mater.*, **2018**, *17*, 119.

578 [30] S. Holliday, R. S. Ashraf, A. Wadsworth, D. Baran, S. A. Yousaf, C. B. Nielsen, C. H.

579 Tan, S. D. Dimitrov, Z. Shang, N. Gasparini, M. Alamoudi, F. Laquai, C. J. Brabec, A.

580 Salleo, J. R. Durrant, I. McCulloch, *Nat. Commun.*, **2016**, *7*, 11585.

581 [31] M. F. Al-Mudhaffer, M. J. Griffith, K. Feron, N. C. Nicolaidis, N. A. Cooling, X. Zhou,

582 J. Holdsworth, W. J. Belcher, P. C. Dastoor, *Sol. Energy Mater. Sol. Cells*, **2018**, *175*,

583 77.

584 [32] M. Li, K. Gao, X. Wan, Q. Zhang, B. Kan, R. Xia, F. Liu, X. Yang, H. Feng, W. Ni, Y.

585 Wang, J. Peng, H. Zhang, Z. Liang, H.-L. Yip, X. Peng, Y. Cao, Y. Chen, *Nat.*

586 *Photonics*, **2017**, *11*, 85.

587 [33] A. Ciavatti, L. Basiricò, I. Fratelli, S. Lai, P. Cosseddu, A. Bonfiglio, J. E. Anthony, B.

588 Fraboni, *Adv. Funct. Mater.*, **2018**, 1806119.

589 [34] W. R. Hendee, R. E. Ritenour, *Medical Imaging Physics*, Wiley-Liss, Inc., New York,

590 **2002**.

591 [35] B. Kim, J. Lee, J. Kang, *J. Instrum.*, **2017**, *12*, C01009.

592 [36] H. Seon, D. Ban, J. Kang, *J. Instrum.*, **2018**, *13*, C11009.

593 [37] D. Anderson, S. Cottam, H. Heim, H. Zhang, N. P. Holmes, M. J. Griffith, *MRS*

594 *Commun.*, **2019**, *9*, 1206.

595 [38] H. Nakamura, Y. Shirakawa, H. Kitamura, T. Yamada, Z. Shidara, T. Yokozuka, P.

596 Nguyen, T. Takahashi, S. Takahashi, *Radiation Measurements*, **2013**, *59*, 172.

597 [39] J. A. Posar, M. Large, J. R. Paino, D. J. Butler, M. J. Griffith, S. Hood, M. L. F. Lerch,

598 A. Rosenfeld, P. J. Sellin, S. Guatelli, M. Petasecca, *J. Synchrotron Radiation*, **2021**,

599 *Under Review*.

600 [40] Y. M. Protopopov, V. G. Vasil'chenko, *Nucl. Instrum. Meth. Phys. Res. B*, **1995**, *95*,

601 496.

602 [41] M. Dettmann, V. Herrig, J. Maldonis, J. Neuhaus, D. Shrestha, P. Rajbhandari, Z.

603 Thune, M. Been, M. Martinez-Szewczyk, V. Khristenko, Y. Onel, U. Akgun, *J.*

604 *Instrum.*, **2017**, *12*, P03017.

605 [42] G. Li, Y. Yang, R. A. B. Devine, C. Mayberry, *Nanotechnology*, **2008**, *19*, 424014: 1.

606 [43] J. Luke, E. M. Speller, A. Wadsworth, M. F. Wyatt, S. Dimitrov, H. K. H. Lee, W. C.

607 T. Zhe Li, I. McCulloch, D. Bagnis, J. R. Durrant, J.-S. Kim, *Adv. Energy Mater.*, **2019**,

608 *9*, 1803755.

609 [44] P. E. Keivanidis, N. C. Greenham, H. Sirringhaus, R. H. Friend, J. C. Blakesley, R.

610 Speller, M. Campoy-Quiles, T. Agostinelli, D. D. C. Bradley, J. Nelson, *Appl. Phys.*

611 *Lett.*, **2008**, *92*.